

# Magnon spectroscopy in the electron microscope

Demie Kepaptsoglou<sup>1,2,3\*†</sup>, José Ángel Castellanos-Reyes<sup>4†</sup>, Adam Kerrigan<sup>2,3</sup>, Júlio Alves do Nascimento<sup>2,3</sup>, Paul M. Zeiger<sup>4</sup>, Khalil El hajraoui<sup>1,2</sup>, Juan Carlos Idrobo<sup>5,6</sup>, Budhika G. Mendis<sup>7</sup>, Anders Bergman<sup>4</sup>, Vlado K. Lazarov<sup>2,3</sup>, Ján Ruzs<sup>4\*</sup>, and Quentin M. Ramasse<sup>1,8,9\*</sup>

<sup>1</sup>*SuperSTEM Laboratory, SciTech Daresbury Campus, Daresbury, WA4 4AD, UK.*

<sup>2</sup>*School of Physics, Engineering and Technology, University of York, Heslington, YO10 5DD, UK.*

<sup>3</sup>*JEOL NanoCentre, University of York, Heslington, YO10 5DD, UK.*

<sup>4</sup>*Department of Physics and Astronomy, Uppsala University, Box 516, Uppsala, 75120, Sweden.*

<sup>5</sup>*Materials Science and Engineering Department, University of Washington, Seattle, WA 98195, USA.*

<sup>6</sup>*Physical and Computational Sciences Directorate, Pacific Northwest National Laboratory, Richland, WA 99354, USA.*

<sup>7</sup>*Department of Physics, Durham University, Durham, DH1 3LE, UK.*

<sup>8</sup>*School of Chemical and Process Engineering, University of Leeds, Leeds, LS2 9JT, UK.*

<sup>9</sup>*School of Physics and Astronomy, University of Leeds, Leeds, LS2 9JT, UK.*

\*Corresponding author(s). E-mail(s): [dmkepap@superstem.org](mailto:dmkepap@superstem.org); [jan.ruzs@physics.uu.se](mailto:jan.ruzs@physics.uu.se); [qmramasse@superstem.org](mailto:qmramasse@superstem.org).

†These authors contributed equally to this work.

## Summary

The miniaturisation of transistors is approaching its limits due to challenges in heat management and information transfer speed [1]. To overcome these obstacles, emerging technologies such as spintronics [2] are being developed, which leverage the electron's spin in addition to its charge. Local phenomena at interfaces or structural defects will greatly influence the efficiency of spin-based devices, making the ability to study and control spin-wave propagation at the nano- and atomic scales a key challenge [3, 4]. The development of high-spatial-resolution tools to probe spin waves, also called magnons, at relevant length-scales is thus essential to understand how their properties are affected by such local features. Here, we show the first experimental detection of bulk THz magnons at the nanoscale using scanning transmission electron microscopy. By employing high-resolution electron energy-loss spectroscopy with hybrid-pixel electron detectors optimised for low acceleration voltages, we successfully overcome the challenges posed by weak signals and identify THz-magnon excitations in a thin NiO nanocrystal. Advanced inelastic electron scattering simulations corroborate our findings. These results open new avenues for detecting magnons, exploring their dispersions and their modifications arising from nanoscale structural or chemical defects. This marks an important milestone in magnonics and presents exciting opportunities for the future development of spintronic devices.

## Main Text

The use of a pure spin current in information transistors is predicted to offer non-volatility, faster data processing, higher integration densities, and lower power consumption [5–7]. These degrees of freedom emerge in quantum materials that exhibit unique spin-dependent properties, including topologically protected spin states [5]. At the same time, recent developments in antiferromagnetic (AFM) spintronics have demonstrated that AFM materials, such as NiO, provide a promising platform for spin injection and transport in the THz domain [8] and spin-torque control [9]. Magnons, the collective excitations of the spin lattice in ferro- and antiferro-magnets, which can be visualised semi-classically as a wave of precessing magnetic moments [10], are fast becoming a cornerstone of quantum technology [11] through newly proposed spin-current- and magnon-based device architectures. Of crucial importance are localised phenomena at the nano- and atomic scales such as the scattering of spin waves at hetero-interfaces and structural defects in materials, which can affect spin injection, spin-wave transmission, spin-torque switching, and spin-to-charge conversion. As a result, the ability to achieve (sub-)nm-resolution magnon detection is currently considered one of the main challenges in the field of magnonics [3, 4].

Electrons as a probe for magnon excitations have been commonly used in the past by surface-

scattering of low-energy electrons in reflection high-resolution electron energy-loss spectroscopy (HREELS), using either spin- or non-polarised electron sources [10, 12–14]. While HREELS allows to probe the energy-momentum dispersion of magnon excitations with high energy resolution, it is limited to the study of surface excitations of ultra-thin films over relatively large length-scales due to the scattering cross-sections, poor spatial resolution, and low penetration depth intrinsic to the technique. Similarly, other experimental approaches widely used to study magnons at high energy and momentum resolutions, such as inelastic neutron scattering [15], time-resolved Kerr microscopy [16], or Brillouin light-scattering [17], are also fundamentally limited to spatial resolutions of hundreds of nanometres. Consequently, magnon information from nanometre-sized features, such as defects and buried interfaces, is not accessible.

Since its first demonstration [18, 19], meV-level (vibrational) electron-energy-loss spectroscopy (EELS) in a scanning transmission electron microscope (STEM) has been developing at a swift pace. Several key experimental milestones have now been achieved: the detection of atomic-level contrast in vibrational signals [20], the spectral signatures of individual impurity atoms [21, 22], spatially resolved measurements on point and line defects in crystalline materials [23, 24] as well as momentum-resolved measurements using nanoscale beams [25–27]. With energy losses due to magnon excitations occupying the same spectral window as phonon vibrational modes, ranging from a few to a few hundred meV in solid-state materials [10, 12–14], the promise of detecting magnons in an electron microscope is exciting from both fundamental research and applications points of view.

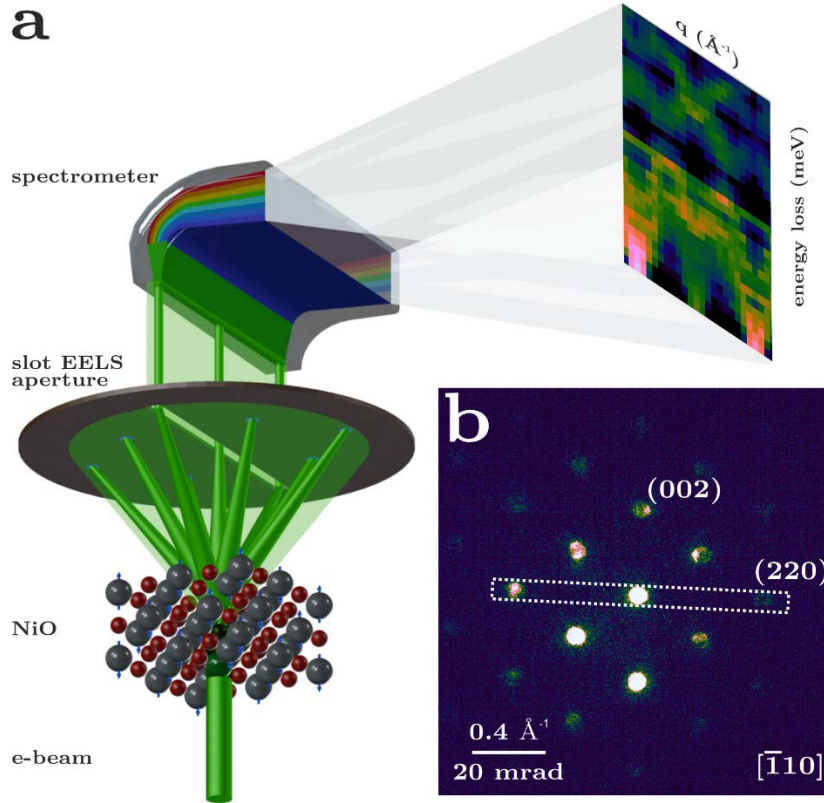
Recent theoretical studies on inelastic magnon scattering in an electron microscope confirmed the feasibility of magnon detection from diffuse inelastic scattering and most importantly demonstrated the tantalising prospect of obtaining atomically localised magnon information [28–30]. This exploratory work also highlighted experimental challenges such as the separation of phonon from magnon diffuse scattering, as the latter is predicted to be several orders of magnitude weaker than the former and yet occupy a similar span of energy losses. Here we tackle the experimental challenges of detecting magnons at the nanoscale using high-resolution EELS in the STEM, and we present the first direct detection of magnons with STEM-EELS. We show that, although challenging, the detection of the inherently weak magnon signal is possible, thanks in part to the dynamic range of hybrid-pixel electron detectors optimized for EELS at low acceleration voltages [31, 32]. The experimental detection of the magnon signal is supported by state-of-the-art numerical simulations of electron scattering [33] underpinned by atomistic spin-dynamics (ASD) simulations [34].

The primary challenge in achieving magnon-EELS is that the energy ranges of phonon and magnon losses overlap, with the weaker magnon signal likely to be overshadowed by the inherently stronger lattice vibration modes. However, these types of losses follow different dispersion relations [35] and,

thus, should be differentiable in momentum-resolved experiments, given a suitable choice of materials systems whose magnon and phonon branches are sufficiently separated in momentum and energy. For this purpose we have selected NiO as a model system; in addition to being a material of interest for spin-transfer-based devices [36], its dispersion relations of phonon and magnon modes have been shown to meet our requirements of momentum and energy separation in the THz range [37, 38].

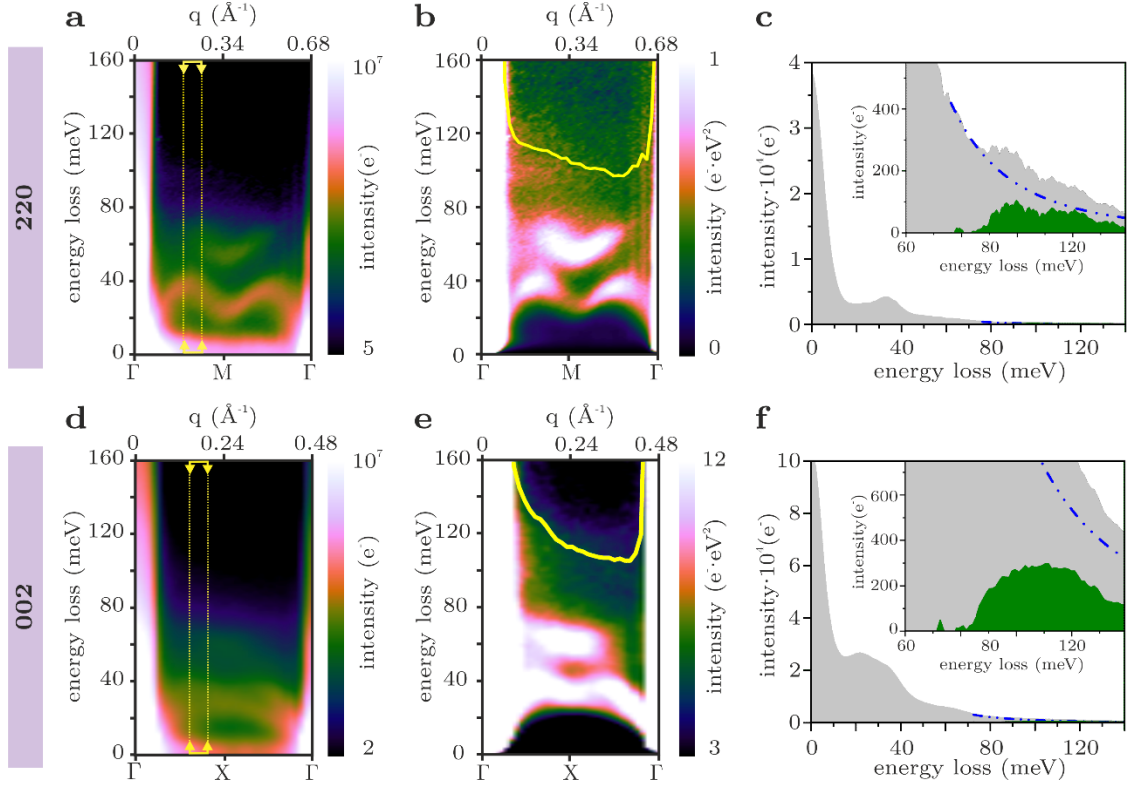
A schematic representation of the experimental geometry used for the momentum-resolved experiments is presented in Fig. 1a. The instrument's electron optics are adjusted to a low convergence angle to form a diffraction-limited nanometre-size electron probe, while achieving sufficient momentum resolution and precision for the experiment (Methods). The electron probe is kept stationary on a region of interest of the NiO crystal, across which the zone-axis orientation is perfectly maintained, estimated to extend no further than a few nanometres from the nominal probe position. The stability of the microscope sample stage, with typical drift performance measured below 0.5 nm per hour, enables hour-long acquisitions on the very same nanometre-sized area of the NiO crystal (Methods). It should be noted that these are still far shorter timescales than necessary for magnon spectroscopy experiments using, e.g., inelastic neutron scattering, where days of integration can be required to record similar datasets from bulk samples. A narrow rectangular (slot) collection aperture for EELS is employed for the angle-resolved measurements [27, 39]. The slot aperture is used to select a row of systematic Bragg reflections (Fig. 1b) and to produce two-dimensional intensity maps of energy loss (or frequency)  $\omega$  versus momentum transfer  $\mathbf{q}$ .

Fig. 2 shows examples of such measurements acquired along the 220 and 002 rows of systematic Bragg reflections in NiO (corresponding to the  $\Gamma \rightarrow M$  and  $\Gamma \rightarrow X$   $\mathbf{q}$ -paths, respectively). Figs 2a,d are the as-acquired intensity maps of energy versus momentum transfer ( $\omega$ - $\mathbf{q}$  maps). For reading clarity the intensity of the maps (calibrated in electrons,  $e^-$ ) is displayed on a logarithmic colour scale. The  $\omega$ - $\mathbf{q}$  maps show two intense bands dispersing around 30 and 50 meV, which correspond to the NiO longitudinal-acoustic (LA) and longitudinal-optical (LO) phonon branches, respectively, in excellent agreement with previous experimental [37] and theoretical work [38, 40]. These are labelled for clarity on Extended Data Figure 2, where gain LA phonon branches are also visible (the higher energy-gain branches are outside of the recorded energy window).



**Fig. 1 | Experimental geometry of momentum-resolved EELS. a.** Schematic representation of the geometry of  $\omega$ - $\mathbf{q}$  vibrational EELS measurements using a rectangular slot collection aperture. **b.** Experimental diffraction pattern along the NiO  $[\bar{1}10]$  zone axis at a 2.25 mrad convergence angle, with the monochromating slit inserted, showing the orientations of the slot EELS collection aperture along the 220 row of systematic Bragg reflections in diffraction space.

Since the intensity of magnon EELS is expected to be significantly lower than that of phonons [28, 30], and given that magnon modes in NiO occur at higher energy losses compared to phonons, the datasets are scaled by the square of the energy loss (intensity  $\times E^2$ ) and presented in Figs. 2b,e. This scaling enhances the visibility of weaker intensity features above the decaying zero-loss-peak tail at higher energy losses in the meV range, while avoiding possible errors in background fitting. After the scaling, a band at approximately 100 meV, already present in the non-scaled data but hard to discern, can be readily observed in maps acquired along  $\Gamma \rightarrow M$  (Fig. 2b). This energy band emerges near the  $\Gamma$ -point and gradually decays in intensity as it approaches the centre of the Brillouin zone; intensity line-profiles along the momentum transfer direction  $\mathbf{q}$  (yellow lines) at an energy loss of 100 meV (averaged over a 20 meV energy width) are drawn as a guide to the eye in Figs. 2b,e to emphasise the presence of this spectral band.



**Fig. 2 | Momentum-resolved vibrational EELS measurements of NiO. a,d.** As-acquired  $\omega$ - $q$  maps along the 220 and 002 rows of reflections, respectively, showing the dispersion of the NiO LA and LO phonon branches, displayed on a logarithmic intensity scale. **b,e.**  $\omega$ - $q$  maps along the same reciprocal space directions scaled by  $E^2$ ; for clarity, superimposed yellow lines show intensity line-profiles of the  $\omega$ - $q$  maps at 100 meV. **c,f.** Integrated spectra at the specific momentum positions marked by arrows in panels a,d.

The observed spectral bands emerge in the same energy and momentum-transfer region where magnon modes are expected for NiO from inelastic-neutron-scattering experiments, albeit blue-shifted by  $\sim 20$  meV. The magnon density of states is known to shift to higher energies with decreasing temperature [41], so this energy difference can be readily accounted for by the difference in acquisition temperatures of the EELS (room temperature) compared to neutron experiments (cryogenic, e.g. 10 K in ref. [37]), a conclusion borne out by the numerical simulations discussed below. Furthermore, the detected bands show an asymmetry along both  $q$ -paths, being more intense close to the Brillouin-zone centre on the left side of panels (a,d) and (b,e) in Fig. 2, consistent with previous neutron-scattering experiments [37, 41]. Here, the very strong asymmetry is also likely due in part to the lower overall experimental spectral intensity away from the direct beam at  $\Gamma$ . In addition, the observed intensity appears most prominent above background further away from  $\Gamma$  in the  $\Gamma \rightarrow X$  direction than along  $\Gamma \rightarrow M$ , again consistent with neutron scattering.

The presence of the weak magnon band at 100 meV in the non-scaled data is confirmed by the

integrated intensity profiles of the  $\omega$ - $\mathbf{q}$  map around a narrow momentum window ( $\Delta q = 0.03 \text{ \AA}^{-1}$ ) in Fig. 2c ( $q = 0.24 \text{ \AA}^{-1}$  along  $\Gamma \rightarrow M$ , marked by yellow arrows and dashed lines in Fig. 2a). This highlights the shape of the peak, with a rising edge from 80 meV reaching a maximum at  $\sim 100$  meV, before a weaker feature extending up to 120 meV. Similarly, the magnon band at  $\sim 100$  meV is observed in the integrated intensity profile of the  $\Gamma \rightarrow X$   $\mathbf{q}$ -path at  $q = 0.17 \text{ \AA}^{-1}$  ( $\Delta q = 0.02 \text{ \AA}^{-1}$  window in Fig. 2d), comparatively further away from the  $\Gamma$  point than the band observed in the  $\Gamma \rightarrow M$  direction.

Due to the overlap of the elastic (or ZLP), phonon and magnon signals along  $\mathbf{q}$  it is difficult to quantify the absolute intensity of the observed energy bands. Nevertheless, an estimate can be given by the integral of the magnon band within the  $\Gamma \rightarrow M \rightarrow \Gamma$  window (excluding  $\Gamma$  points); after subtraction of a power-law background used to model the decaying intensity tail underlying the LO phonon signal (inset in Fig. 2c), the integrated magnon intensity is estimated  $\sim 8.5 \times 10^4 e^-$ . For comparison, the corresponding integrated phonon intensity (for both LA and LO branches) over the same  $\Delta q$  is three orders of magnitude higher,  $\sim 2.0 \times 10^7 e^-$ , while the total integrated intensity across the entire rectangular slot aperture, assumed to be representative of the total beam intensity impinging on the sample, was  $5.2 \times 10^9 e^-$ , in good agreement with expected relative intensities of the weak magnon and total scattered EELS signals [28]. A similar intensity analysis holds for the  $\Gamma \rightarrow X$  data.

To support our experimental findings, we have performed first-principles calculations of momentum-resolved phonon and magnon EELS using parameters that carefully reflect the experimental conditions, in particular in terms of sample temperature, magnetic environment, and the microscope's electron optical parameters (Methods). Figure 3 summarises the results of the simulations for both  $\mathbf{q}$ -paths studied in the experiments. We observe phonon EELS dispersions presenting bands reaching up to about 70 meV for both  $\mathbf{q}$ -paths, with a small gap at around 40 meV (see Fig. 3a,c). This qualitatively matches with the two dominant features observed in the experimental momentum-resolved EELS datasets (the LA and LO phonon branches), albeit with a somewhat higher energy-loss gap at about 50 meV. Due to the very long acquisition times required to reveal the emergence of the magnon bands, and the chosen balance between momentum and spatial resolution arising from the 2.25 mrad probe convergence angle, some experimental spectral smearing obscures the finer details of the experimental phonon dispersion in comparison to the calculations. For completeness, a better resolved  $\omega$ - $\mathbf{q}$  map is presented in the Extended Data Figure 2 comparing very favourably with the calculated phonon dispersion in Fig. 3a (but in which the magnon signal is less readily visible due to shorter integration times). The relatively rich pattern observed in phonon EELS simulations is in contrast with magnon EELS simulations, which display only negligible fractional scattering intensities at energy losses below *ca.* 60 meV, with two broad yet well-isolated peaks at energy losses between 90-120 meV (Figs. 3b,d).

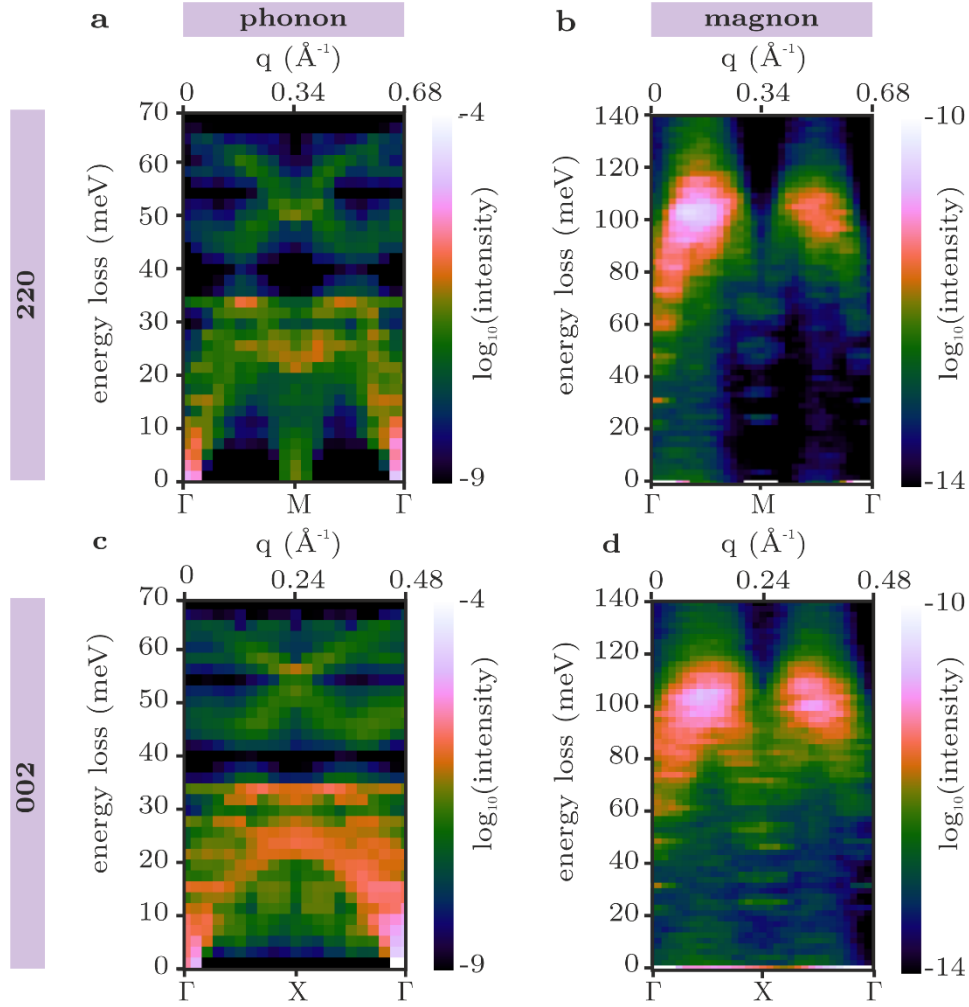


**Fig. 3 | Calculated vibrational and magnon EELS of NiO.** Simulated EELS dispersion curves of (a,c) phonon and (b,d) magnon excitations, along the  $\Gamma \rightarrow M$  and  $\Gamma \rightarrow X$   $q$ -paths of the Brillouin zone for NiO, respectively. Experimental parameters such as sample temperature, environmental magnetic field inside the microscope and electron optical parameter are considered (Methods).

The theoretical calculations match the features emerging above the phonon EELS background observed in experiments, Fig. 2. The maximum simulated magnon intensity appears around 100 meV, as observed experimentally, whereas identical (exploratory) simulations at lower temperature, not shown here, predict an energy-loss peak close to 120 meV, as expected from neutron experiments carried out at 10 K. The measured asymmetry along the momentum axis, also present in neutron-scattering data, is well reproduced, showing a considerably higher intensity for the magnon EELS peak closer to the  $\Gamma$ -point in the centre of the diffraction plane, when compared to the peak near the 220 or 002  $\Gamma$ -points, respectively. This is intrinsic to the magnon EELS scattering strength, although as discussed above, it will be exacerbated experimentally due to the much lower intensity away from the direct electron beam in STEM-EELS experiments. Similarly, along the momentum direction, the calculated magnon intensity maximum appears comparatively closer to the X-point than to the M-



point. Furthermore, the intensity in the energy-loss direction matches the experimental observations, with an extended spectral tail towards 120 meV in the  $\Gamma \rightarrow M$  calculations, compared to a slightly more rounded peak centred at 100 meV in the  $\Gamma \rightarrow X$  case. This excellent match between experiment and theory further strengthens the interpretation of the intensities observed experimentally around 100 meV as being the spectral signature of scattering arising from magnon excitations in the nanometre-sized NiO crystal probed by the electron beam.

## Discussion and Conclusions

Our observation of magnon excitations in STEM-EELS arrives a decade after the milestone report of the detection of phonons in an electron microscope [18]. One may reasonably expect further developments of magnon EELS to follow a similar trajectory and pace as its phonon spectroscopy counterpart, with a clear blueprint to attempt studies of magnon dispersions and their nano-scale modifications in the vicinity of surfaces, interfaces or defects. These will create a radical new way of studying magnetism, spin magnetic ordering and spin wave excitations at the length-scales relevant for device fabrication. In this context we emphasise that our measurements have been performed with a probe diameter of less than 2 nm, with the region of interest estimated to be tens of nanometres in size at most, across which the NiO crystal was perfectly on axis to enable a careful probing of the chosen diffraction directions, as illustrated by the overview and high-resolution images of the crystal area used for the experiments along the 002 row of reflections in Extended Data Figure 1.

The significantly lower cross-section for scattering of fast electrons from magnon excitations compared to phonons [28, 29, 33] remains a challenge for the development of this technique. In our experiments, calculations suggest that we can expect to detect one electron scattered by magnons only every 1-2 seconds, while there can be hundreds or thousands of phonon-scattered electrons every second under equivalent experimental settings. Due to this, it is unlikely that with current detector technologies magnon dispersions can be unambiguously determined in the presence of phonon branches within the same region of  $\omega$ - $\mathbf{q}$  space, placing a restriction on the number of materials systems for which the direct observation of magnon peaks will be possible in the immediate future. However, alternative strategies may be deployed to enable a less direct detection of magnons in STEM-EELS, in particular in cases for which magnons and phonon branches are close. The interaction of magnons with other excitations in the same energy range can give rise to other types of quasiparticles such as magnon polarons (the hybridised coupled state between a phonon and a magnon), which could act as a less challenging spectroscopic fingerprint. These interactions are characterised by modifications of the observed dispersion diagrams (e.g., changes in dispersive behaviour, or the appearance of spectral band anti-crossings), or to the spectral bands dependence

on temperature [42, 43]. Preliminary reports suggest this strategy, although indirect, may be less demanding on signal sensitivity [44, 45]. Similarly, the different dependence on temperature or other external sample stimuli of magnons compared to phonons may provide an efficient means to disentangle the weak magnon signal from higher intensity features [30].

Nevertheless, our experiments emphasize again how new technological and methodological developments in STEM-EELS are opening exciting experimental avenues. Electron counting detectors enable EELS measurements hampered only by Poisson noise [46]. Although comparatively shorter signal integration and experimental duration is an advantage for the STEM-EELS approach, the exceptional stability of STEM instruments with low sample drift, operating at reduced acceleration voltages minimizing sample damage [47], combined with advanced data acquisition procedures such as multi-frame recording [48], make it possible in principle to significantly increase acquisition times, approaching scales that are common in other experimental techniques such as angle-resolved photoemission (ARPES) [49] or inelastic neutron scattering, while retaining higher spatial resolutions at the nano- or atomic scales. With the increasing availability of advanced tools like variable magnetic pole pieces [50] and liquid-helium-temperature stages [51], along with newer generations of high-resolution monochromators, future magnon STEM-EELS experiments will gain new controls over magnetic field and extended temperature ranges. These can be used to suppress magnon or phonon modes or enhance energy separation, marking a new era for magnonics studies at the nanometre scale.

## References

- [1] Mamaluy, D. & Gao, X. The fundamental downscaling limit of field effect transistors. *Applied Physics Letters* **106**, 193503 (2015). <https://doi.org/10.1063/1.4919871>.
- [2] Wolf, S. A. *et al.* Spintronics: A spin-based electronics vision for the future. *Science* **294**, 1488–1495 (2001). <https://www.science.org/doi/abs/10.1126/science.1065389>.
- [3] Barman, A. *et al.* The 2021 Magnonics Roadmap. *Journal of Physics: Condensed Matter* **33**, 413001 (2021). <https://iopscience.iop.org/article/10.1088/1361-648X/abec1a>.
- [4] Flebus, B. *et al.* The 2024 magnonics roadmap. *Journal of Physics: Condensed Matter* **36**, 363501 (2024). <https://dx.doi.org/10.1088/1361-648X/ad399c>.
- [5] Chumak, A. V., Serga, A. A. & Hillebrands, B. Magnonic crystals for data processing. *Journal of Physics D: Applied Physics* **50**, 244001 (2017). <https://dx.doi.org/10.1088/1361-6463/aa6a65>.
- [6] Puebla, J., Kim, J., Kondou, K. & Otani, Y. Spintronic devices for energy-efficient data storage and energy harvesting. *Communications Materials* **1**, 24 (2020). <https://doi.org/10.1038/s43246-020-0022-5>.
- [7] Han, W., Otani, Y. & Maekawa, S. Quantum materials for spin and charge conversion. *npj*

- Quantum Materials* **3**, 27 (2018). <https://www.nature.com/articles/s41535-018-0100-9>.
- [8] Rezende, S. M., Azevedo, A. & Rodríguez-Suárez, R. L. Introduction to anti-ferromagnetic magnons. *Journal of Applied Physics* **126**, 151101 (2019). <https://doi.org/10.1063/1.5109132>.
- [9] Moriyama, T., Oda, K., Ohkochi, T., Kimata, M. & Ono, T. Spin torque control of antiferromagnetic moments in NiO. *Scientific Reports* **8**, 14167 (2018). <https://doi.org/10.1038/s41598-018-32508-w>.
- [10] Vollmer, R., Etzkorn, M., Anil Kumar, P., Ibach, H. & Kirschner, J. Spin-polarized electron energy loss spectroscopy: a method to measure magnon energies. *Journal of Magnetism and Magnetic Materials* **272-276**, 2126–2130 (2004). <https://doi.org/10.1016/j.jmmm.2003.12.506>.
- [11] Flebus, B., Rezende, S. M., Grundler, D. & Barman, A. Recent advances in magnonics. *Journal of Applied Physics* **133**, 160401 (2023). <https://doi.org/10.1063/5.0153424>.
- [12] Zakeri, K., Zhang, Y. & Kirschner, J. Surface magnons probed by spin-polarized electron energy loss spectroscopy. *Journal of Electron Spectroscopy and Related Phenomena* **189**, 157–163 (2013). <https://doi.org/10.1016/j.elspec.2012.06.009>.
- [13] Rajeswari, J. *et al.* Surface spin waves of fcc cobalt films on Cu(100): High-resolution spectra and comparison to theory. *Physical Review B* **86**, 165436 (2012). <https://doi.org/10.1103/PhysRevB.86.165436>.
- [14] Ibach, H., Bocquet, F. C., Sforzini, J., Soubatch, S. & Tautz, F. S. Electron energy loss spectroscopy with parallel readout of energy and momentum. *Review of Scientific Instruments* **88**, 033903 (2017). <https://doi.org/10.1063/1.4977529>.
- [15] Shirane, G., Minkiewicz, V. J. & Nathans, R. Spin Waves in 3d Metals. *Journal of Applied Physics* **39**, 383–390 (1968). <https://doi.org/10.1063/1.2163453>.
- [16] Keatley, P. S. *et al.* A platform for time-resolved scanning Kerr microscopy in the near-field. *Review of Scientific Instruments* **88**, 123708 (2017). <https://doi.org/10.1063/1.4998016>.
- [17] Sebastian, T., Schultheiss, K., Obry, B., Hillebrands, B. & Schultheiss, H. Micro- focused Brillouin light scattering: imaging spin waves at the nanoscale. *Frontiers in Physics* **3**, 35 (2015). <https://www.frontiersin.org/journals/physics/articles/10.3389/fphy.2015.00035>.
- [18] Krivanek, O. L. *et al.* Vibrational spectroscopy in the electron microscope. *Nature* **514**, 209 (2014). <https://doi.org/10.1038/nature13870><http://10.0.4.14/nature13870>.
- [19] Miyata, T. *et al.* Measurement of vibrational spectrum of liquid using monochromated scanning transmission electron microscopy-electron energy loss spectroscopy. *Microscopy* **63**, 377 (2014). <https://doi.org/10.1093/jmicro/dfu023>.
- [20] Hage, F. S., Kepaptsoglou, D. M., Ramasse, Q. M. & Allen, L. J. Phonon Spectroscopy at Atomic

- Resolution. *Physical Review Letters* **122**, 016103 (2019).  
<https://link.aps.org/doi/10.1103/PhysRevLett.122.016103>.
- [21] Hage, F. S., Radtke, G., Kepaptsoglou, D. M., Lazzeri, M. & Ramasse, Q. M. Single-atom vibrational spectroscopy in the scanning transmission electron microscope. *Science* **367**, 1124–1127 (2020). <https://doi.org/10.1126/science.aba1136>.
- [22] Xu, M. *et al.* Single-atom vibrational spectroscopy with chemical-bonding sensitivity. *Nature Materials* **22**, 612–618 (2023). <https://www.nature.com/articles/s41563-023-01500-9>.
- [23] Yan, X. *et al.* Single-defect phonons imaged by electron microscopy. *Nature* **589**, 65–69 (2021). <https://doi.org/10.1038/s41586-020-03049-y>.
- [24] Hoglund, E. R. *et al.* Emergent interface vibrational structure of oxide superlattices. *Nature* **601**, 556–561 (2022). <https://www.nature.com/articles/s41586-021-04238-z>.
- [25] Hage, F. S. *et al.* Nanoscale momentum-resolved vibrational spectroscopy. *Science Advances* **4**, eaar7495 (2018). <https://www.science.org/doi/10.1126/sciadv.aar7495>.
- [26] Senga, R. *et al.* Position and momentum mapping of vibrations in graphene nanostructures. *Nature* **573**, 247–250 (2019). <https://www.nature.com/articles/s41586-019-1477-8>.
- [27] Qi, R. *et al.* Four-dimensional vibrational spectroscopy for nanoscale mapping of phonon dispersion in BN nanotubes. *Nature Communications* **12**, 1179 (2021). <https://doi.org/10.1038/s41467-021-21452-5>.
- [28] Lyon, K. *et al.* Theory of magnon diffuse scattering in scanning transmission electron microscopy. *Physical Review B* **104**, 214418 (2021). <https://doi.org/10.1103/PhysRevB.104.214418>.
- [29] Mendis, B. Quantum theory of magnon excitation by high energy electron beams. *Ultramicroscopy* **239**, 113548 (2022). <https://doi.org/10.1016/j.ultramic.2022.113548>.
- [30] Castellanos-Reyes, J. Á. *et al.* Unveiling the impact of temperature on magnon diffuse scattering detection in the transmission electron microscope. *Physical Review B* **108**, 134435 (2023). <https://link.aps.org/doi/10.1103/PhysRevB.108.134435>.
- [31] Plotkin-Swing, B. *et al.* Hybrid pixel direct detector for electron energy loss spectroscopy. *Ultramicroscopy* **217**, 113067 (2020). <https://doi.org/10.1016/j.ultramic.2020.113067>.
- [32] Fernandez-Perez, S. *et al.* Characterization of a hybrid pixel counting detector using a silicon sensor and the IBEX readout ASIC for electron detection. *Journal of Instrumentation* **16**, P10034 (2021). <https://dx.doi.org/10.1088/1748-0221/16/10/P10034>.
- [33] Castellanos-Reyes, J. Á., Zeiger, P. & Rusz, J. Dynamical theory of angle-resolved electron energy loss and gain spectroscopies of phonons and magnons including multiple scattering effects. *arXiv preprint arXiv:2401.15599* (2024). <http://arxiv.org/abs/2401.15599>.

- [34] The Uppsala atomistic spin dynamics code, UppASD. <https://github.com/UppASD/UppASD> (2023). Last accessed 2023-11-13.
- [35] Wu, X., Liu, Z. & Luo, T. Magnon and phonon dispersion, lifetime, and thermal conductivity of iron from spin-lattice dynamics simulations. *Journal of Applied Physics* **123**, 85109 (2018). <https://doi.org/10.1063/1.5020611>.
- [36] Baldrati, L. *et al.* Spin transport in multilayer systems with fully epitaxial NiO thin films. *Physical Review B* **98**, 14409 (2018). <https://doi.org/10.1103/PhysRevB.98.014409>.
- [37] Sun, Q. *et al.* Mutual spin-phonon driving effects and phonon eigenvector renormalization in nickel (II) oxide. *Proceedings of the National Academy of Sciences* **119**, e2120553119 (2022). <https://pnas.org/doi/full/10.1073/pnas.2120553119>.
- [38] Betto, D. *et al.* Three-dimensional dispersion of spin waves measured in NiO by resonant inelastic x-ray scattering. *Physical Review B* **96**, 020409 (2017). <https://doi.org/10.1103/PhysRevB.96.020409>.
- [39] Fossard, F. *et al.* Angle-resolved electron energy loss spectroscopy in hexagonal boron nitride. *Physical Review B* **96**, 115304 (2017). <https://doi.org/10.1103/PhysRevB.96.115304>.
- [40] Gupta, B. R. K. & Verma, M. P. Application of three body force shell model to the lattice dynamics of transition metal oxides MnO, CoO and NiO. *Journal of Physics and Chemistry of Solids* **38**, 929–932 (1977). [https://doi.org/10.1016/0022-3697\(77\)90133-0](https://doi.org/10.1016/0022-3697(77)90133-0).
- [41] Woo, C. H., Wen, H., Semenov, A. A., Dudarev, S. L. & Ma, P.-W. Quantum heat bath for spin-lattice dynamics. *Physical Review B* **91**, 104306 (2015). <https://doi.org/10.1103/PhysRevB.91.104306>.
- [42] Godejohann, F. *et al.* Magnon polaron formed by selectively coupled coherent magnon and phonon modes of a surface patterned ferromagnet. *Physical Review B* **102**, 144438 (2020). <https://link.aps.org/doi/10.1103/PhysRevB.102.144438>.
- [43] Olsson, K. S. *et al.* Spin-phonon interaction in yttrium iron garnet. *Physical Review B* **104**, L020401 (2021). <https://link.aps.org/doi/10.1103/PhysRevB.104.L020401>.
- [44] Reifsnnyder, A. *et al.* Detecting Magnon-Phonon Coupling in the Scanning Transmission Electron Microscope. *Microscopy and Microanalysis* **30**, ozae044.772 (2024). <https://doi.org/10.1093/mam/ozae044.772>.
- [45] El hajraoui, K. *et al.* Towards the In-situ Detection of Spin Charge Accumulation at a Metal/Insulator Interface Using STEM-EELS Technique. *Microscopy and Microanalysis* **28**, 2338–2339 (2022). <https://doi.org/10.1017/S1431927622008972>.
- [46] Hart, J. L. *et al.* Direct detection electron energy-loss spectroscopy: A method to push the limits of resolution and sensitivity. *Scientific Reports* **7**, 8243 (2017).

<https://doi.org/10.1038/s41598-017-07709-4>.

- [47] Krivanek, O. L. *et al.* Gentle STEM: ADF imaging and EELS at low primary energies. *Ultramicroscopy* **110**, 935–945 (2010). <https://doi.org/10.1016/j.ultramic.2010.02.007>.
- [48] Jones, L. *et al.* Optimising multi-frame ADF-STEM for high-precision atomic- resolution strain mapping. *Ultramicroscopy* **179**, 57–62 (2017). <https://doi.org/10.1016/j.ultramic.2017.04.007>.
- [49] Iwasawa, H. *et al.* Accurate and efficient data acquisition methods for high-resolution angle-resolved photoemission microscopy. *Scientific Reports* **8**, 17431 (2018).  
<https://doi.org/10.1038/s41598-018-34894-7>.
- [50] Shibata, N. *et al.* Atomic-resolution electron microscopy in a magnetic field free environment. *Nature Communications* **10**, 2308 (2019). <https://doi.org/10.1038/s41467-019-10281-2>.
- [51] Rennich, E., Sung, S. H., Agarwal, N., Hovden, R. & El Baggari, I. Liquid Helium TEM Sample Holder with High Stability and Long Hold Times. *Microscopy and Microanalysis* **29**, 1696–1697 (2023).  
<https://doi.org/10.1093/micmic/ozad067.874>.

## Methods

### *Materials and Specimen Preparation*

Electron microscopy specimens were prepared conventionally from a commercially available NiO single crystal substrate (Surface Preparation Laboratory) by crushing (pestle and mortar), dispersing in chloroform and drop casting on standard lacey carbon support grids. Additional specimens were prepared by focused ion beam (FIB), using a Hitachi NX5000 Ethos triple-beam instrument, from a 30 nm-thick NiO thin film grown on an yttrium-stabilised zirconia (YSZ) substrate. Sample thickness was estimated using the standard log-ratio method from low-loss EELS spectra to be approximately 40 nm in the areas used for all data presented here. Grains with a suitable zone-axis orientation were specifically chosen so their diffraction patterns aligned close to the main axis of the slot aperture for momentum-resolved acquisitions. Small rotational adjustments were carried out using the microscope's projector lens system, to ensure perfect alignment of the row of diffraction spots to the slot axis. When this was not possible, the sample was removed from the microscope and rotated to match the measured rotation of pre-screened grains of interest. The effective regions of interest across which the crystal areas were both thin enough, overhanging any lacey carbon support material, and perfectly on zone axis (judged from the symmetry of the observed intensities in the diffraction pattern), were estimated to be no larger than 10 nm across in most cases.

### *High Resolution Electron Energy Loss Spectroscopy and data processing*

High-resolution electron energy loss spectroscopy (EELS) measurements were performed in a Nion UltraSTEM 100MC "Hermes" aberration-corrected dedicated scanning transmission electron microscope. The instrument is equipped with a Nion-designed high-resolution ground-potential monochromator, a Nion Iris high-energy-resolution energy-loss spectrometer and a Dectris ELA hybrid-pixel direct electron detector optimized for EELS at low acceleration voltages [52]. The instrument was operated at 60 kV acceleration voltage, with the electron optics adjusted to achieve a 2.25 mrad convergence angle corresponding to  $\sim 1.3$  nm electron probe diameter (Extended Data Figure 1). The energy resolution was 7.2 meV, set by the position of the monochromator energy-selection slit and estimated by the full-width at half-maximum of the zero-loss peak (ZLP) in vacuum (Extended Data Figure 2). The resulting probe current after monochromation and with the optical parameters chosen to ensure the highest achievable energy resolution was  $\sim 1$  pA. For the momentum-resolved experiments, a rectangular (slot) aperture (0.125 mm  $\times$  2 mm) was employed, with the projector optics adjusted to match the full angular size of the beam to the width of the slit, yielding a momentum resolution  $\Delta q = 0.009 \text{ \AA}^{-1}$ . The slot aspect-ratio allows an angular range in the momentum direction of 50 mrad. The spectrometer dispersion was set to 1.0 or 0.5 meV/channel (002

and 220 acquisitions, respectively). Each  $\omega$ - $q$  dataset was a multi-frame acquisition of the whole 2-dimensional extent of the spectrometer camera. A typical dataset comprised 15,000 frames, using an exposure time of 75 ms per frame, resulting in an acquisition time of 22 min per single dataset (limited only by the data-export capabilities of the microscope operating software). The multi-frame stacks were subsequently assessed for energy drift, aligned using rigid image registration, and integrated. The final data presented here are sums of multiple such integrated datasets acquired consecutively (necessary as explained above due to data-size-handling limitations) from the same specimen area, on the same day and under identical experimental conditions. No other post-processing was applied. Specifically, the dataset in Fig. 2a is the sum of 90,000 individual camera frames, acquired along the  $[\bar{1}10]$  zone axis of NiO (Fig. 1b) with a dwell time of 75 ms, corresponding to a total of 2 h acquisition time. Due to the integration and averaging of multiple datasets, some spectral smearing results in an effective energy resolution for the experiment of 9.2 meV, measured by the full-width at half-maximum (FWHM) of the zero-loss peak (ZLP) in the final integrated dataset. The dataset in Fig. 2d is the sum of 60,000 individual camera frames, acquired along the  $[100]$  zone axis of NiO (Extended Data Figure 1) with a dwell time of 75 ms, corresponding to a total of 1.2 h acquisition time. The effective energy resolution of the experiment was 11 meV, measured by the full-width at half-maximum (FWHM) of the zero-loss peak (ZLP) in the integrated dataset.

### ***Theoretical calculations***

**Magnon EELS simulations.** The numerical simulations were performed following the methodology described in Ref. [33], capturing both single- and multiple-scattering processes and dynamical diffraction effects. Specifically, the momentum-resolved EELS signals were computed as the time-to-energy Fourier transform of the temperature-dependent time auto-correlation of the electron beam wave function obtained from the multislice method. Atomistic spin dynamics (ASD) simulations in UppASD [34] were conducted on a  $16 \times 16 \times 96$  supercell (of dimensions 6.672 nm  $\times$  6.672 nm  $\times$  40.032 nm) of NiO cubic unit cells, using the experimental parameters reported in Ref. [53]. For the spin-Hamiltonian parameters, we used the values from the bottom row of Table III in Ref. [53]. Given that we utilised a cubic cell, the nearest-neighbour exchange interaction  $J_1$  was set as the average of  $J_1^+$  and  $J_1^-$  from the same row. To account for the effect of the microscope's objective lens on the sample environment, a 1.5 T static external magnetic field oriented along the  $[001]$  direction was included. Oxygen atoms were excluded from the ASD simulations due to their negligible magnetic moment. Employing a Gilbert damping  $\alpha = 5 \times 10^{-4}$  and a time step of 0.1 fs, a thermalisation phase of 70,000 steps was followed by a 7.813 ps trajectory at 300 K for generating snapshots every 13 fs, enabling the exploration of magnon frequencies up to 159 meV. Note that from ASD simulations we determined that the employed parameters of the spin-Hamiltonian predict a Néel temperature of



304 K, instead of the known experimental value of 523 K. Therefore, in our calculations we employed an effective temperature  $T_e = 174.4$  K, since  $300 \text{ K} = T_e (523/304)$ . In total, 602 snapshots were generated and the magnon EELS signal was obtained as the average over 16 sets of 151 consecutive snapshots mutually offset by 30 snapshots. Each set spanned 1.963 ps, providing an energy resolution of 2.1 meV. The electron-beam exit wave functions were computed using the Pauli multislice method on a numerical grid of  $1344 \times 1344$  points with 4032 slices across the NiO supercell's thickness, including the oxygen atoms (with a zero magnetic moment). A 60 kV electron probe with a 2.25 mrad convergence semi-angle, propagating along the [001] direction, was employed. We have used the parametrised magnetic fields and vector potentials developed in Ref. [54]. The Debye-Waller factor (from Table S.V in the supplemental material of Ref. [55]) and the absorptive optical potential (see appendix B of Ref. [30]) were included to simulate, in a first approximation, the effect of phonon excitations on elastic scattering.

**Phonon EELS calculations.** We have used the frequency-resolved frozen phonon multi-slice method (FRFPMS) [56] with 34 frequency bins spanning a range from 0 THz up to 17 THz in 0.5 THz-wide intervals. Within each of the frequency bins, we have averaged over 128 structure snapshots. The supercell size for FRFPMS simulations was  $10 \times 10 \times 98$  cubic Bravais unit cells of NiO. For phonon EELS, a conventional multislice algorithm was used, as implemented in the DrProbe code [57], using a numerical grid of  $840 \times 840 \times 784$  pixels. Convergence semi-angle, acceleration voltage, and aperture shape were all set according to the experimental geometry.

In contrast to previous applications of the FRFPMS method, we did not use molecular dynamics to generate snapshots of the vibrating structure. Instead, we first performed density functional theory (DFT) simulations of the phonon eigenmodes (see below). Using this information, we have generated structure snapshots in an approach following Refs. [58, 59] by calculating atomic displacements due to random excitation of phonon modes following their thermal population at 300 K. However, instead of summing over all the phonon modes, we have split them by their eigen-frequencies into the above-mentioned 34 frequency bins and generated sets of 128 snapshots for each frequency bin separately. Considering the small unit cell of NiO, this approach brings DFT-level precision at a lower computational cost than training a machine-learning inter-atomic potential for subsequent molecular dynamics simulations.

**Density functional theory calculations.** DFT calculations were performed using VASP [60] at the meta-GGA level using the  $r^2$ SCAN functional [61] with the PAW pseudo-potentials [62] containing the kinetic-energy density of core electrons. A  $2 \times 2 \times 2$  supercell of the conventional standard  $Fm\bar{3}m$  unit cell of NiO was geometrically optimised; the cell shape, cell volume, and atomic positions were allowed to relax to a tolerance of  $1 \text{ meV}/\text{\AA}$ , to capture the distortion away from the cubic symmetry caused by

antiferromagnetic ordering along the [111] direction. For all calculations, a  $\Gamma$ -centred  $k$ -point grid with spacing  $2\pi(0.06) \text{ \AA}^{-1}$  was used with a plane-wave cut-off of 750 eV. The python package phonopy [63, 64] was used to generate the displacements required to calculate force constants in a  $4 \times 4 \times 4$  supercell of the conventional standard unit cell. The dielectric constant and Born effective charges were also calculated in a  $4 \times 4 \times 4$  supercell using the finite differences approach. These are for use in the non-analytical correction [65, 66], required due to the polar nature of NiO.

Phonon modes were sampled on a grid of  $5 \times 5 \times 49$   $q$ -points spanning the Brillouin zone of a  $2 \times 2 \times 2$  supercell of NiO used in DFT simulations for calculation of the force matrix. The grid was chosen in a way to guarantee that atomic displacements are periodic across the boundaries of the simulation supercell used in phonon EELS simulations (see above).

### Data availability

The data that support the findings of this study are available from the corresponding authors upon reasonable request. All the codes used in this work are available from the corresponding authors upon reasonable request.

### Additional References

- [52] Krivanek, O. L. *et al.* Progress in ultrahigh energy resolution EELS. *Ultramicroscopy* **203**, 60–67 (2019). <https://doi.org/10.1016/j.ultramic.2018.12.006>.
- [53] Hutchings, M. T. & Samuelsen, E. J. Measurement of spin-wave dispersion in NiO by inelastic neutron scattering and its relation to magnetic properties. *Physical Review B* **6**, 3447–3461 (1972). <https://link.aps.org/doi/10.1103/PhysRevB.6.3447>.
- [54] Lyon, K. & Rusz, J. Parameterization of magnetic vector potentials and fields for efficient multislice calculations of elastic electron scattering. *Acta Crystallographica Section A: Foundations and Advances* **77**, 509–518 (2021). <https://doi.org/10.1107/S2053273321008792>.
- [55] Lee, S. *et al.* Magnetoelastic coupling forbidden by time-reversal symmetry: Spin-direction-dependent magnetoelastic coupling on MnO, CoO, and NiO. *Physical Review B* **93**, 064429 (2016). <https://link.aps.org/doi/10.1103/PhysRevB.93.064429>.
- [56] Zeiger, P. M. & Rusz, J. Efficient and Versatile Model for Vibrational STEM- EELS. *Physical Review Letters* **124**, 025501 (2020). <https://doi.org/10.1103/PhysRevLett.124.025501>.
- [57] Barthel, J. Dr. Probe: A software for high-resolution STEM image simulation. *Ultramicroscopy* **193**, 1–11 (2018). <https://doi.org/10.1016/j.ultramic.2018.06.003>.
- [58] A. Muller, D., Edwards, B., J. Kirkland, E. & Silcox, J. Simulation of thermal diffuse scattering including a detailed phonon dispersion curve. *Ultramicroscopy* **86**, 371–380 (2001). [https://doi.org/10.1016/S0304-3991\(00\)00128-5](https://doi.org/10.1016/S0304-3991(00)00128-5).

- [59] Chen, X., Kim, D. S. & LeBeau, J. M. A comparison of molecular dynamics potentials used to account for thermal diffuse scattering in multislice simulations. *Ultramicroscopy* **244**, 113644 (2023). <https://doi.org/10.1016/j.ultramic.2022.113644>.
- [60] Kresse, G. & Furthmüller, J. Efficient iterative schemes for ab initio total-energy calculations using a plane-wave basis set. *Physical Review B* **54**, 11169–11186 (1996). <https://link.aps.org/doi/10.1103/PhysRevB.54.11169>.
- [61] Furness, J. W., Kaplan, A. D., Ning, J., Perdew, J. P. & Sun, J. Accurate and Numerically Efficient r<sup>2</sup>SCAN Meta-Generalized Gradient Approximation. *The Journal of Physical Chemistry Letters* **11**, 8208–8215 (2020). <https://doi.org/10.1021/acs.jpcllett.0c02405>.
- [62] Kresse, G. & Joubert, D. From ultrasoft pseudopotentials to the projector augmented-wave method. *Physical Review B* **59**, 1758–1775 (1999). <https://doi.org/10.1103/PhysRevB.59.1758>.
- [63] Togo, A. First-principles Phonon Calculations with Phonopy and Phono3py. *Journal of the Physical Society of Japan* **92**, 12001 (2023). <https://doi.org/10.1103/PhysRevB.59.1758>.
- [64] Togo, A., Chaput, L., Tadano, T. & Tanaka, I. Implementation strategies in phonopy and phono3py. *Journal of Physics: Condensed Matter* **35**, 353001 (2023). <https://dx.doi.org/10.1088/1361-648X/acd831>.
- [65] Gonze, X. & Lee, C. Dynamical matrices, Born effective charges, dielectric permittivity tensors, and interatomic force constants from density-functional perturbation theory. *Physical Review B* **55**, 10355–10368 (1997). <https://doi.org/10.1103/PhysRevB.55.10355>.
- [66] Gonze, X., Charlier, J.-C., Allan, D. C. & Teter, M. P. Interatomic force constants from first principles: The case of  $\alpha$ -quartz. *Physical Review B* **50**, 13035–13038 (1994). <https://doi.org/10.1103/PhysRevB.50.13035>.

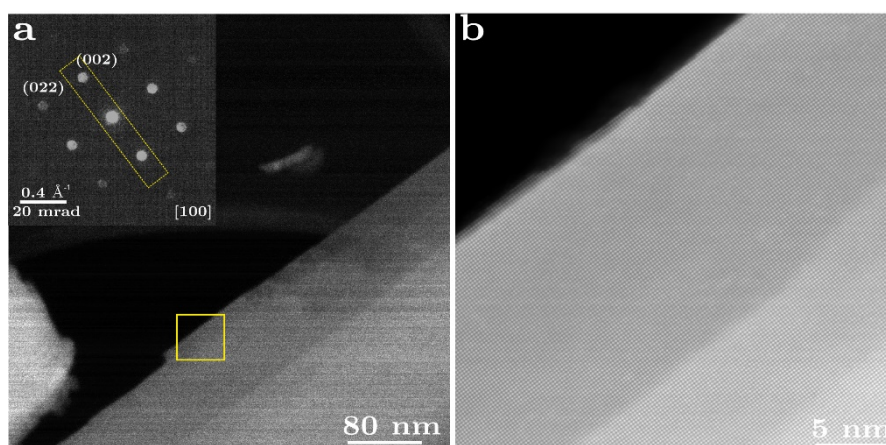
**Acknowledgements.** SuperSTEM is the National Research Facility for Advanced Electron Microscopy supported in part by the Engineering and Physical Sciences Research Council (EPSRC) under grant number EP/W021080/1. We acknowledge further financial support from the EPSRC via grants number EP/V048767/1, EP/Z531194/1, EP/V036432/1, as well as the Royal Society via grant no. IES/R1/211016. We acknowledge the Swedish Research Council (grant no. 2021-03848), Olle Engkvist’s foundation (grant no. 214-0331), STINT (grant no. CH2019-8211), Knut and Alice Wallenberg Foundation (grant no. 2022.0079), and eSENCE for financial support. The simulations were enabled by resources provided by the National Academic Infrastructure for Supercomputing in Sweden (NAISS) and the Swedish National Infrastructure for Computing (SNIC) at NSC Centre partially funded by the Swedish Research Council through grant agreements no. 2022-06725 and no. 2018-05973.

**Author contributions.** DMK and QMR designed, performed experiments and analysed the experimental results. JCI analysed the experimental results. JACR, PZ, AB and JR designed and

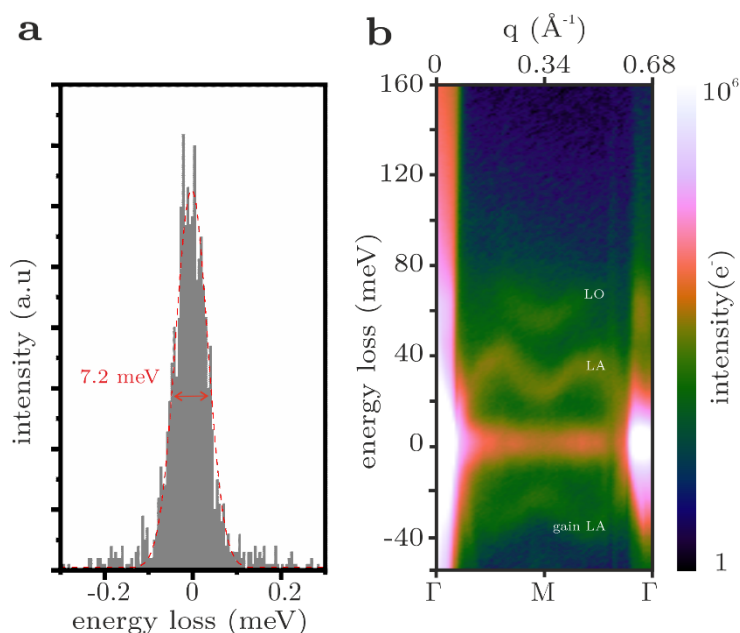
performed magnon calculations. AK, JdN, JR, PZ, BM and VL designed and performed phonon calculations. KEH prepared samples for analysis. All authors contributed equally to the analysis, interpretation and preparation of the manuscript.

**Competing interests.** The authors declare no competing interests.

## Extended Data Figures



**Extended Data Figure 1 | Imaging of the NiO sample.** *a.* Annular dark-field image of a NiO sample acquired with a 2.25 mrad convergence angle ( $\sim 1.3$  nm probe) along the [100] zone axis. Inset: experimental diffraction pattern along the NiO [100] zone axis at a 2.25 mrad convergence angle, with the monochromating slit inserted, showing the orientation of the EELS collection slot aperture along the (002) row of reflections. *b.* Atomic-resolution high-angle annular-dark-field STEM (HAADF-STEM) image acquired using a 31 mrad convergence angle from the area marked with a white rectangle in panel *a*.



**Extended Data Figure 2 | Vibrational EELS measurements of NiO.** *a.* EELS spectrum corresponding to a single acquisition frame (75 ms) in vacuum, showing a ZLP measuring 7.2 meV at the FWHM. *b.* As-acquired  $\omega$ - $q$  maps along 220 row of NiO reflections, displaying the dispersion of the NiO LA / LO phonon branches, as well as the LA gain branch, presented on a logarithmic intensity scale. The dataset corresponds to 15,000 integrated frames (75 ms each).